Regularized Higher-Order In Vivo Shimming

Dong-Hyun Kim,[1,2*] Elfar Adalsteinsson,[1] Gary H. Glover,[1] and Daniel M. Spielman[1]

A regularized algorithm is presented for localized in vivo shimming. The technique uses first- (*X,Y,Z*), second- (Z^2, *ZX, ZY,* X^2-Y^2, *XY*), and third-order (Z^3) shim coils, and is robust when applied to arbitrarily-shaped, as well as off-center, regions of interest (ROIs). A single-shot spiral pulse sequence is used for rapid field map acquisition, and a least-squares calculation of the shim currents is performed to minimize the root-mean-square (RMS) value of the B_0 inhomogeneity over a user-selected ROI. The use of a singular value decomposition (SVD) in combination with a regularization algorithm significantly improves the numerical stability of the least-squares fitting procedure. The fully automated shimming package is implemented on a 3 T GE Signa system and its robust performance is demonstrated in phantom and in vivo studies. Magn Reson Med 48:715–722, 2002. © 2002 Wiley-Liss, Inc.

Key words: higher-order shimming; singular value decomposition; regularization; magnetic field homogeneity; in vivo shimming

Magnetic resonance spectroscopy (MRS) and many MRI methods benefit from a well-shimmed magnetic field. For standard gradient-echo imaging sequences, a well-shimmed field can limit geometric distortions due to phase errors, and signal dropouts due to intravoxel dephasing. Most fat and water imaging techniques benefit from a homogeneous magnetic field, and fast imaging sequences such as echo planar, spiral, and projection MRI are all sensitive to off-resonance effects. In addition, the success of in vivo MRS studies critically depends on the spatial homogeneity of the magnetic field over the selected region of interest (ROI).

While there are many different approaches to in vivo shimming, the common overall goal is to compute the desired corrective fields over the ROI and apply the necessary corrective currents as offsets to the imaging gradients (1–3) or to the higher-order shim coils. The use of higher-order (typically, second-order and Z^3) shims provides additional benefit to both brain (4) and body imaging (5). To calculate the desired shim currents, Gruetter et al. (6,7) described a method in which six projections of the magnetic field are mapped and fitted to a mathematical model for each shim. Alternatively, methods that acquire 3D field maps to calculate the corrective currents over the ROI have also been employed (8,9). To increase the overall speed of the shimming process, field maps have been obtained using one of several different rapid imaging techniques (10–12).

While in vivo shimming has been carefully investigated in the above-mentioned studies, there are several aspects that limit its efficacy. The region over which good homogeneity is required may be away from the isocenter of the magnet, leading to interactions between shims (13). For example, in a situation where a Z shim correction is needed over a small off-center ROI, such correction can also be produced by any order of Z shim, including Z^2 and Z^3. The problem of finding the correct shim values becomes ill-conditioned and can lead to a demand for excessive currents in the other shim channels, especially when measurement noise is present, or when the size of the ROI goes to zero, thereby leading to increased interactions. The use of such higher-order shims to produce a Z correction is inefficient and expensive in terms of heat production, hence some means of discriminating against such unwanted interactions is needed. The situation typically becomes particularly difficult when shimming in vivo because of finite SNR, limited spatial resolution of the field maps, and motion artifacts. These limitations often lead to numerical instabilities in which drastic changes in shim currents have little effect on the overall homogeneity across the ROI. Therefore, it is important for a robust shimming algorithm to avoid these situations that would otherwise lead to excessive power usage to the shim coils, and could exceed the capabilities of the hardware. In this work, a regularization algorithm is shown to limit maximum shim currents by avoiding situations in which shims are played against each other.

In the following sections, we describe our automated higher-order shimming package. First, we introduce the theory of a regularized algorithm for localized shimming based on a singular value decomposition (SVD) of a field reference matrix. Then, we demonstrate the numerical stability of our method and give representative results from various applications that are particularly sensitive to B_0 inhomogeneity.

THEORY

SVD Algorithm and Error Perturbation

To determine the optimal shim currents, a field reference matrix and a field map of the object being scanned are collected using the sequence described in the Methods section. The field reference matrix connects the field produced at each spatial position with the currents for each shim coil. Thus, each column in the matrix represents the field values produced by a given shim coil. These values are collected only once when setting up the shimming package. The field map is a vector of field values at each spatial position throughout the sample.

Once the user has determined the shimming ROI, only those points that correspond to the ROI are extracted from

[1]Radiological Sciences Laboratory, Department of Radiology, Stanford University, Stanford, California.

[2]Department of Electrical Engineering, Stanford University, Stanford, California.

Grant sponsor: GE Medical Systems; Grant sponsor: NIH; Grant numbers: CA 48269; RR09784; CA79944-01; AG18947; DAMD17-99-1-9385.

*Correspondence to: Dong-Hyun Kim, Lucas MRS Imaging Center, Stanford, CA 94305-5488. E-mail: dhkim@stanford.edu

Received 29 August 2001; revised 19 June 2002; accepted 24 July 2002.
DOI 10.1002/mrm.10267
Published online in Wiley InterScience (www.interscience.wiley.com).

both the field reference matrix and the field map of the object in order to work with a much smaller matrix equation. Optimal shim currents are obtained via a least-squares solution of the equation

$$\mathbf{Mi} = \mathbf{b} \quad [1]$$

where **M** is an $n \times 10$ matrix extracted from the field reference matrix, n is the number of points extracted within the ROI, **b** is a vector containing the extracted points from the measured field map of the object, and **-i** is a 10×1 vector of the desired shim currents corresponding to the center frequency, three first-order gradients (*X, Y,* and *Z*) and six higher-order shims (*XY, ZX, ZY,* X^2-Y^2, Z^2, and Z^3). The solution is obtained by an SVD of the matrix **M**

$$\mathbf{M} = \mathbf{UWV}^{\mathbf{T}} = \sum_{j=1}^{r} \sigma_j \mathbf{u_j} \mathbf{v_j}^{\mathbf{T}} \quad [2]$$

where Rank(**M**) = r, **W** = diag($\sigma_1 \ldots \sigma_r$), **U** = [$\mathbf{u}_1 \ldots \mathbf{u}_r$], **V** = [$\mathbf{v}_1 \ldots \mathbf{v}_r$]. The solution of Eq. [1] can be found via a pseudo inverse of **M**. Thus,

$$\mathbf{i} = \mathrm{M}^{+}\,\mathrm{b} = \sum_{j=1}^{r} \frac{\mathrm{u_j}^{\mathrm{T}}\mathrm{b}}{\sigma_j}\mathrm{v_j} \quad [3]$$

where $\mathbf{M}^{+}$ is the pseudo inverse of **M** ($\mathbf{M}^{+} = \mathbf{VW}^{-1}\mathbf{U}^{T}$). However, depending on the shape and location of the selected ROI, the condition number, $\kappa(\mathbf{M})$, of the matrix **M** can be large, leading to an ill-conditioned matrix. This situation implies that two or more shims have interacting effects within the selected ROI. As mentioned, for an off-center ROI, increased shim interactions are commonly observed.

The effects of a large condition number are readily determined by considering the cases of error in the acquired field map **b**, and also error in the field reference matrix M. First, an error in the field map, which we call $\delta\mathbf{b}$, will propagate into the solution, **i**, by

$$\frac{\|\delta\mathbf{i}\|}{\|\mathbf{i}\|} \leq \kappa(\mathbf{M}) \frac{\|\delta\mathbf{b}\|}{\|\mathbf{b}\|} \quad [4]$$

where $\|\cdot\|$ is the l_2 norm for a vector and the largest singular value for a matrix. Thus, an error in the field map ($\delta\mathbf{b}$) can lead to error in the calculated shim currents ($\delta\mathbf{i}$) that is proportional to the condition number of the field reference matrix, possibly leading to an unstable solution. Likewise, an error in the field reference matrix, which we call $\delta\mathbf{M}$, will propagate into the solution current by

$$\frac{\|\delta\mathbf{i}\|}{\|\mathbf{i} + \delta\mathbf{i}\|} \leq \kappa(\mathrm{M}) \frac{\|\delta\mathbf{M}\|}{\|\mathbf{M}\|}. \quad [5]$$

From Eqs. [4] and [5], it can be seen that even small errors in the field reference matrix or the field map of the object can lead to significant shimming errors when the ROI is such that the condition number of **M** is large. This will also affect the RMS of the residual norm. An expression for the above two cases is given by (14)

$$\|\delta\mathbf{r}\| \leq \frac{\|\delta\mathbf{M}\|}{\|\mathbf{M}\|}\|\mathbf{i}\|\|\mathbf{M}\| + \|\delta\mathbf{b}\| + \frac{\|\delta\mathbf{M}\|}{\|\mathbf{M}\|}\kappa(\mathbf{M})\|\mathbf{r}\| \quad [6]$$

where **r** is the residual when no errors are present (**r** = **Mi-b**), and $\delta\mathbf{r}$ is the residual error when errors are present in both the field map of the object and the field reference matrix.

Regularization

Inverse problems with ill-conditioned matrices are prone to unstable solutions, and numerical methods, known as regularization, are often employed to cope with these situations. Various regularization methods exist for inverting ill-conditioned matrices. Examples are the Tikhonov regularization (15), the damped SVD (DSVD) regularization method (16), the truncated SVD (TSVD) method (17), and the thresholding method (18). We considered several of these choices, and two of these methods, namely the thresholding method and a modified version of the TSVD, were implemented and evaluated on our system. Figure 1 illustrates the performance of various regularization methods by plotting the solution norm (the amount of current needed for shimming) vs. the residual norm (the RMS value of the field homogeneity achievable) for an ROI chosen to be the frontal lobe of the brain.

In our implementation of the thresholding method, the singular values of the matrix **M** were truncated to give a condition number below an empirically determined threshold. However, the nature of the condition number depends not only on the orthogonality of the shims themselves, but also on the ROI selected. For example, in shimming the frontal lobe, results were stable when singular values were truncated to achieve a condition number below 50. Other ROIs could require different threshold values.

In the modified version of the TSVD, the values of σ_j, $|\mathbf{u_j}^{\mathbf{T}}\mathbf{b}|$, and $|\mathbf{u_j}^{\mathbf{T}}\mathbf{b}/\sigma_j|$ are determined, and corresponding singular values with high $|\mathbf{u_j}^{\mathbf{T}}\mathbf{b}/\sigma_j|$ values are truncated. From Eq. [3], it is seen that corresponding singular values with large $|\mathbf{u_j}^{\mathbf{T}}\mathbf{b}/\sigma_j|$ contribute significantly to the norm of the solution. A large solution norm could require correction currents to be bigger than the value used for the generation of the field reference matrix. If the variance of the field reference is σ^2_{ref}, and the current offset used to generate the matrix is ΔC_{ref}, the standard deviation (SD) of the corrected field would be proportional to (9)

$$\frac{\Delta c}{\Delta c_{ref}}\sigma_{ref} \quad [7]$$

where Δc is the required correction current. Thus, a high solution norm can lead to unstable performance. Although eliminating the singular values with large $|\mathbf{u^T_j b}/\sigma_j|$ decreases the solution norm ($\|\mathbf{i}\|$), the trade-off comes from the residual norm ($\|\mathbf{r}\|$). The residual norm, which gives the RMS value of the shimming capability, is determined by $|\mathbf{u_j}^{\mathbf{T}}\mathbf{b}|$ since this is the projection on to the desired output

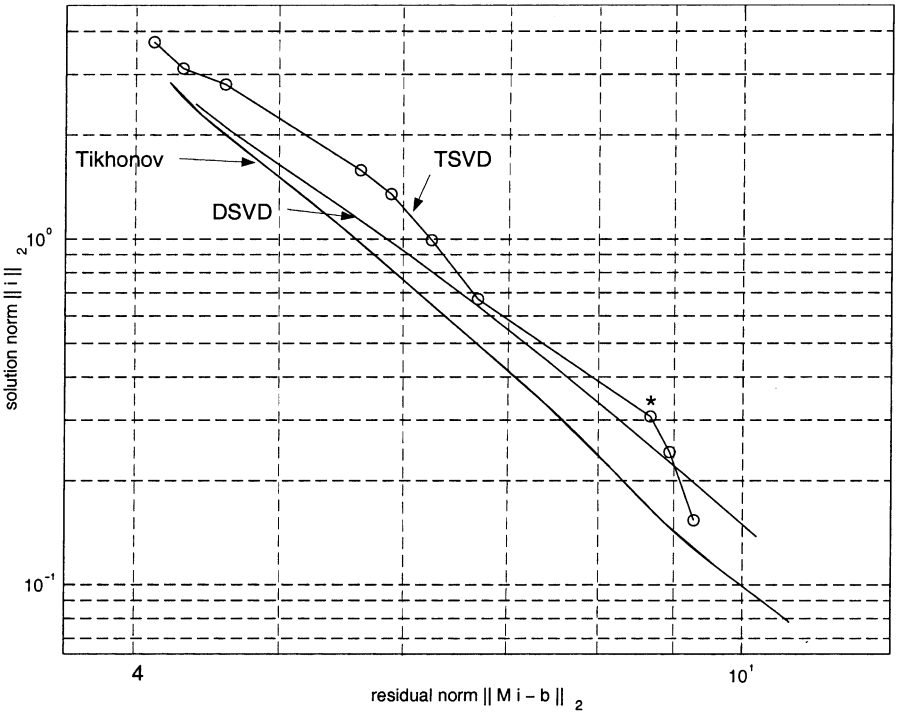

FIG. 1. The solution norm (amount of current needed) vs. the residual norm (RMS value of the field) from three regularization methods applied to the same in vivo data. The ROI was chosen to be the frontal lobe of the brain. All three methods give similar results in terms of solution vs. residual norm trade-off. Depending on the ROI, the curve does not necessarily become convex, which can lead to difficulty in finding the desired optimal solution.

b. Removing any singular value will degrade the RMS of the residual field, especially those with high $|\mathbf{u_j}^T\mathbf{b}|$. Therefore, a reasonable solution is to include singular values that significantly reduce the residual norm without greatly increasing the solution norm. This method of regularization is illustrated in Fig. 2. The values of σ_j, $|\mathbf{u_j}^T\mathbf{b}|$, and $|\mathbf{u_j}^T\mathbf{b}/\sigma_j|$ for each singular values are plotted. In this example, the 8th, 9th, and 10th singular values are discarded due to their large values of $|\mathbf{u_j}^T\mathbf{b}/\sigma_j|$.

METHODS

For field map measurements, phase difference images were obtained using two single-shot gradient-recalled

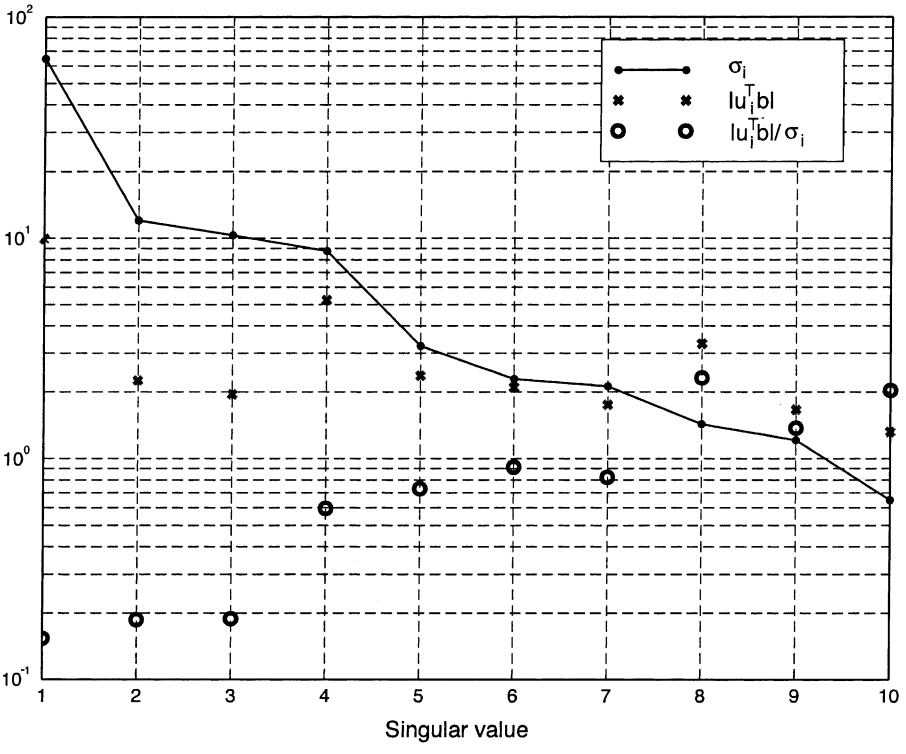

FIG. 2. A plot of σ_j, $|\mathbf{u_j}^T\mathbf{b}|$, and $|\mathbf{u^T_j b}/\sigma_j|$ vs. the *j*th singular value for the data in Fig. 1. This plot is used to eliminate certain singular values. The 8th, 9th, and 10th singular values are truncated due to the relatively large values of $|\mathbf{u^T_j b}/\sigma_j|$. Truncating the 8th singular value will increase the residual norm since it depends inversely on the projection vector $|\mathbf{u^T_j b}|$. (Note the increased residual norm in Fig. 1 for TSVD after truncating the 8th singular value indicated by *.)

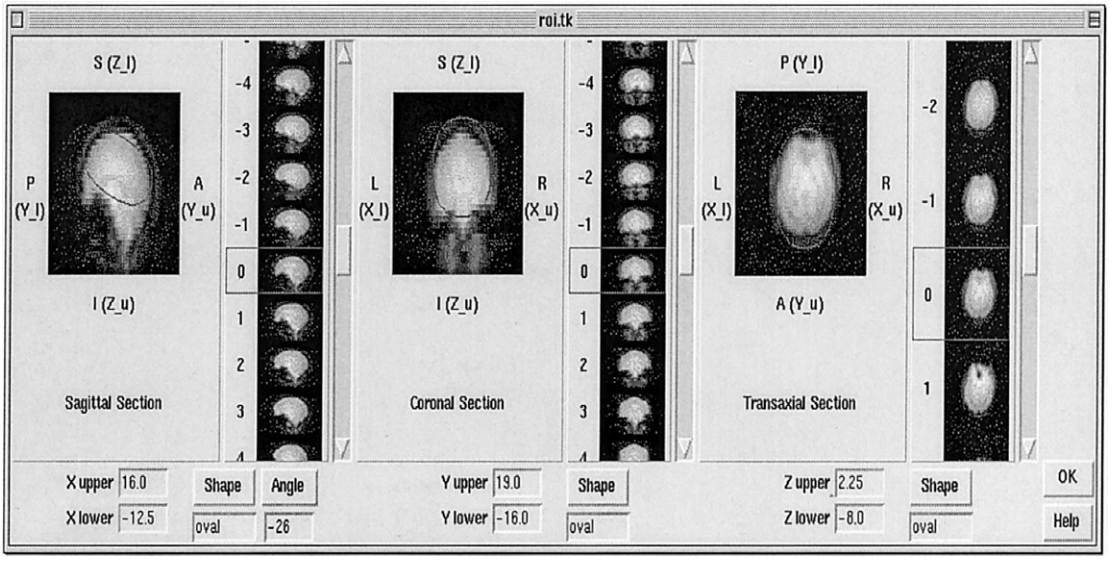

FIG. 3. A screen shot of the ROI selection interface. The complete shimming procedure was packaged into a graphic interface. This portion shows the user's selection of ROI. The images are updated after each scan.

echo (GRE) multislice spiral acquisitions (19) with an echo time (TE) delay between acquisitions of 2 ms. A spectral-spatial excitation pulse was used to eliminate fat signals and avoid undesired phase wrapping. We acquired a 3D field reference matrix using a water-filled sphere (28 cm diameter) over a $32 \times 32 \times 24$ cm field of view (FOV) with $32 \times 32 \times 32$ pixel resolution. All scans were performed with a GE Signa 3 T scanner with maximum gradient amplitude of 3.5 G/cm and slew rate of 20 G/cm/ms. The data acquisition readout for a single-shot spiral was 5.3 ms, and the total scan time for the 32 slices was 4 s (TR/TE = 1000/7 ms, flip angle = 60°).

The field reference matrix was acquired for three first-order gradients (*X, Y,* and *Z*) and six higher-order shims (*XY, ZX, ZY,* X^2-Y^2, Z^2, and Z^3). For each shim, an offset current was chosen as the largest value that did not show a phase wrap or significant signal dropout. This offset current value was set as the reference current for that shim. After all the shim currents and the corresponding field maps were determined, the reference field matrix was constructed by reordering the field maps, corresponding to each shim term, into a vector which then formed a column of the final reference matrix. Hence, these vectors serve as basis functions for the least-squares algorithm. A constant term representing the center frequency was also added to this matrix. Given that the field reference matrix only needs to be acquired once on a given scanner, eight signal averages were used for increased SNR. A detailed description of acquiring the field reference matrix is given by Webb et al. (9).

Field maps of a given object or subject to be shimmed were obtained using the same sequence and timing parameters as described above, without averaging. An ROI was selected by the operator, and corresponding portions from the field reference matrix and the object field map were extracted to form Eq. [1]. A magnitude image was also generated and used as a mask to eliminate areas within the ROI that had insufficient signal intensity. Optimal shim currents were calculated using the described regularization algorithm and then downloaded to the shim power supply upon the user's request.

A graphical user interface was developed which permits easy selection of the ROI and allows the entire shimming procedure to be automated. Figure 3 shows a screen shot of the ROI-selection interface. One iteration of the entire shimming process (field map acquisition, ROI selection, shim computation and downloading) takes approximately 20 s.

RESULTS

Figure 4 shows the RMS field homogeneity values achieved for two different experiments with and without the previously described thresholding regularization. These data illustrate that, without regularization, divergence can be observed even on the first iteration (left). This instability comes from the selected ROI and also depends on factors such as the initial homogeneity, field map errors, and limited SNR. For more general usage, the modified TSVD method was used throughout the rest of the experiments.

An initial study, which compared using just the first-order shim terms vs. using both first- and higher-order shim terms, was conducted with six normal volunteers. The average RMS field deviation was 26.5 ± 1.6 Hz when only first-order shims were used. In contrast, using the three first-order terms in combination with six higher-order terms achieved an average RMS field deviation of 16.5 ± 1.3 Hz. The average field deviation before any shimming was 61.2 ± 3.2 Hz.

Figure 5 shows the achieved RMS value from 10 volunteers. The ROI was selected to be an oblique, off-center ellipsoid covering the upper part of the brain. The achieved average RMS value was approximately 0.15 ppm (18 Hz) at 3 T, and in each case the RMS value converged due to the regularization algorithm.

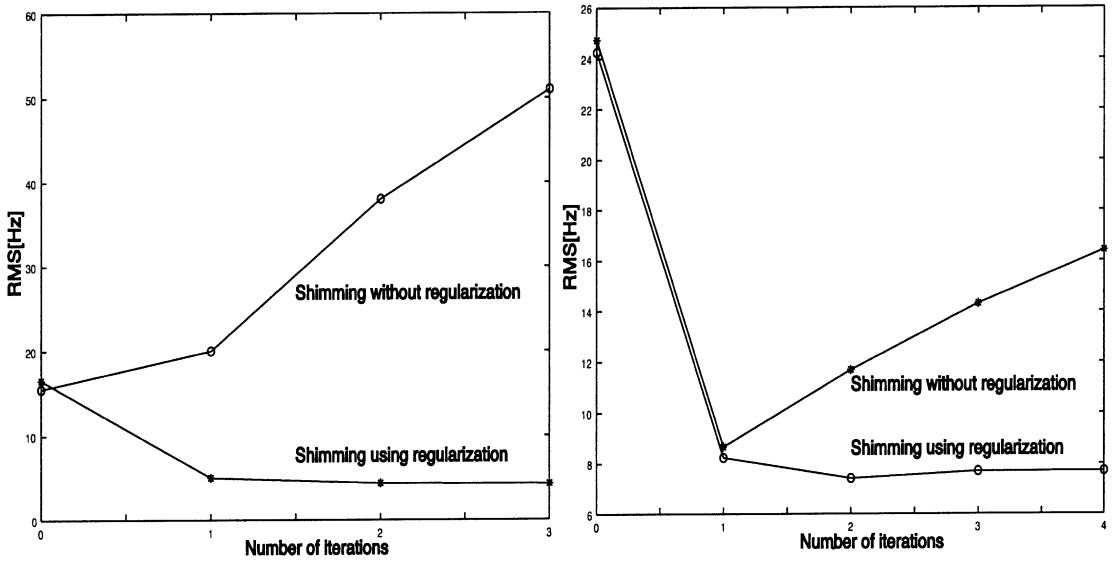

FIG. 4. Comparison of repeated higher-order shimming with and without regularization. The RMS field deviation vs. the number of iterations of the shimming procedure are shown for two different off-center ROIs selected from a spherical phantom. The use of regularization diminishes the deleterious effects of interacting shims that are often exacerbated by poor initial homogeneity and noise in the field maps.

Figure 6 shows spectra from a single-voxel in vivo spectroscopy study in which the ROI is off-center. Compared with first-order shimming, less lipid contamination, improved water suppression, and narrower metabolite linewidth are observed with higher-order shimming.

Figure 7 illustrates decreased artifacts when using higher-order shimming with a single-shot echo-planar imaging (EPI) sequence. For each slice, the geometric distortion due to B_0 inhomogeneity is reduced through the use of higher-order shims.

DISCUSSION

Our results demonstrate the successful implementation of in vivo higher-order shimming using regularization methods, and that such methods are particularly useful in shimming off-center ROIs. The regularization algorithm prevents the computed shim currents from diverging by keeping the solution norm small without large sacrifices in the shimming performance. Additionally, the use of a spiral acquisition sequence for field mapping combined with a

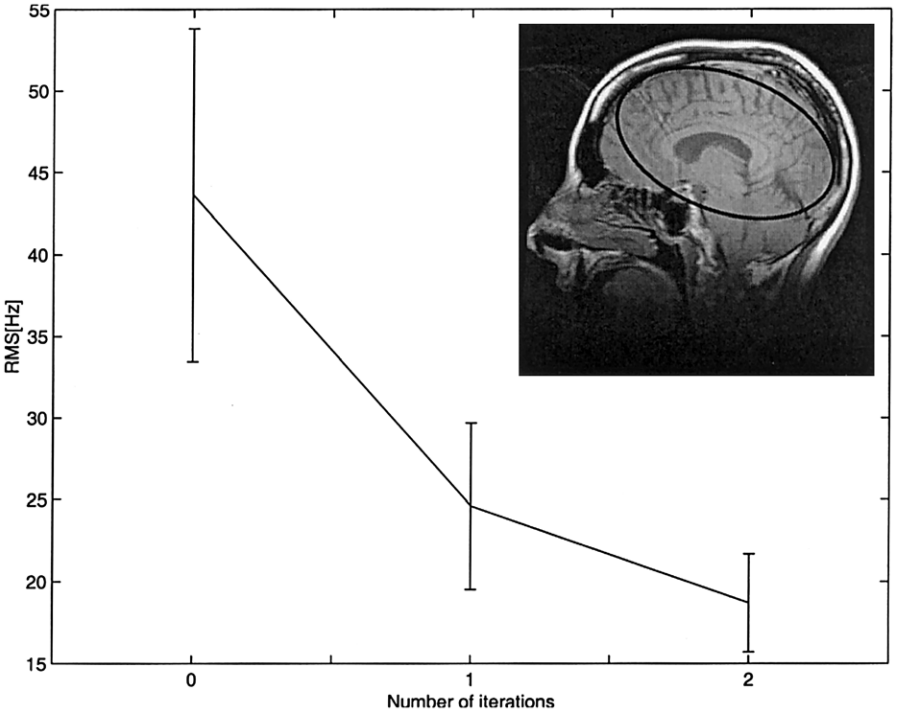

FIG. 5. Results from 10 volunteers following higher-order shimming at 3 T. For each of the cases, the ROI was chosen to be an oblique ellipsoid covering most of the brain, as shown by the inset image. All studies showed significant improvement and rapid convergence. After two shim iterations, the achieved average RMS value was approximately 0.15 ppm (18 Hz at 3 T).

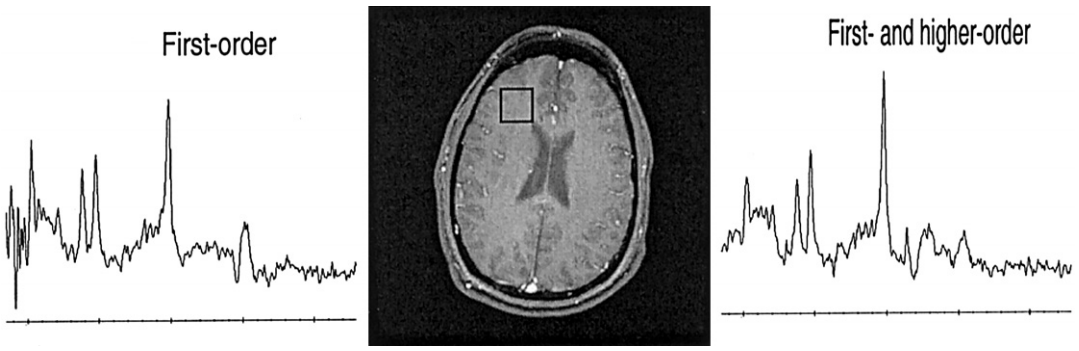

FIG. 6. Spectra obtained from a ^{1}H MRS study using first-order (left) and first- and higher-order (right) shim terms. The single voxel acquisitions were performed using print resolved spectroscopy (PRESS) excitation with chemical shift selective saturation (CHESS) water suppression and the following acquisition parameters: TR/TE = 1500/35 ms, 8 *cc* voxel. The scout scan and the selected ROI are shown in the center.

user-friendly graphical interface allows one iteration of the whole shimming procedure to be executed in about 20 s.

The major sources of error are the measurement noise in the field reference matrix and the field map of the object being shimmed. The field reference matrix, acquired only once during installation, was obtained using eight averages to maximize SNR. The SNR of our field reference matrix was approximately 50:1. Although shim coils are designed to produce fields whose spatial variation may be described by spherical harmonics, the actual fields produced are not guaranteed to be orthogonal even for centered spherical ROIs due to, for example, manufacturing specifications or acquisition errors. Table 1 illustrates the non-orthogonality of the shims on our 3 T scanner by calculating the cross-correlation coefficients of the field values produced by each pair of shims over the whole centered spherical volume of our calibrated field reference matrix. Note the cross-correlation between the Z and Z^3 shims, which was high compared to the cross-correlation coefficients acquired from other sites using the same protocol. The comparison was also made with a field map generated using spherical harmonic functions. In this case, the field map is 'ideal' since it follows the true mathematical equations describing the static magnetic fields produced (20). The correlation coefficients between the ideal field map and our field reference matrix for each shim are .99(X), .99(Y), .99(Z), .86(ZY), .95(X^2-Y^2), .96(ZX), .86(XY), .20(Z^3), and .72(Z^2). This indicates the possible presence of a systematic error in our Z^3 shim coil, and also reflects the non-orthogonality of the shims. The proposed regularized shimming procedure remains robust even in the presence of such errors. Because the field values produced by the shims might not truly reflect their representative harmonic functions, the use of calibrated field reference matrix can be advantageous compared to the use of mathematical representations for field values as the basis func-

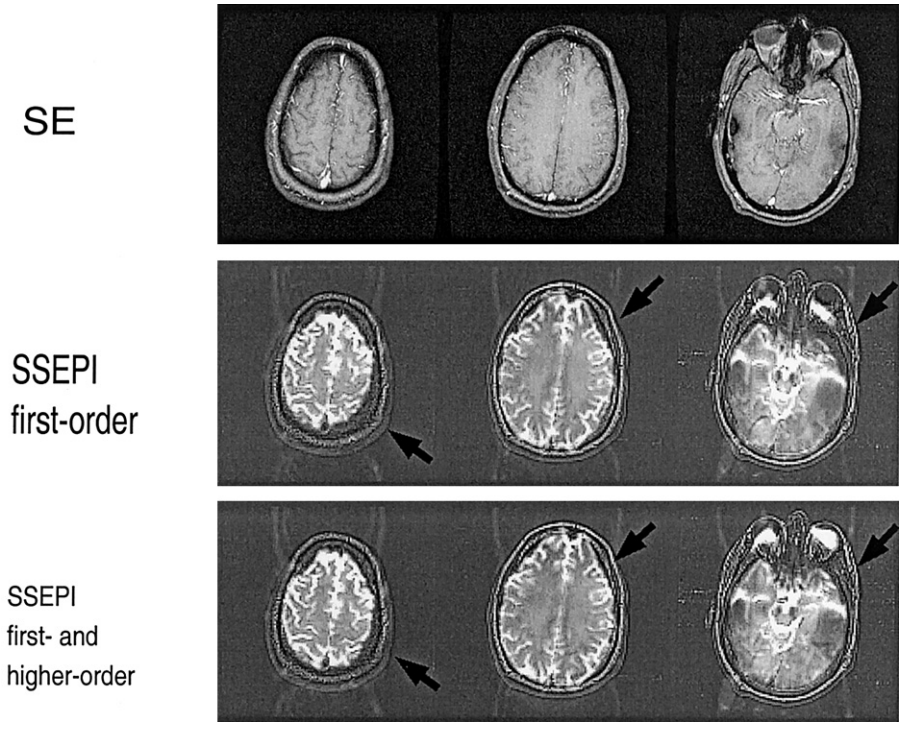

FIG. 7. Single-shot EPI images (2nd and 3rd row) overlaid with an edge-detected version of a conventional spin-echo image (top row) for improved visualization of spatial distortion artifacts. Note that the geometric distortion tends to shrink the image in the anterior/posterior (AP) direction. Distortions are decreased with the use of higher-order shims (FOV/size = 24 cm/128 × 128).

Table 1
Orthogonality of Shims*

	X	Y	Z	XY	ZX	ZY	$X^2–Y^2$	Z^3	Z^2
X	1.0000	0.1627	0.0696	0.2463	0.1283	0.1781	0.1153	0.0856	0.0758
Y		1.0000	0.0632	0.1350	0.2065	0.2585	0.1481	0.1039	–0.0168
Z			1.0000	0.0634	0.0766	–0.0017	0.1583	0.5257	0.0761
XY				1.0000	0.1260	0.1892	0.1583	0.0643	0.1133
ZX					1.0000	0.1517	0.1421	0.1012	0.1075
ZY						1.0000	0.1723	–0.0113	0.0879
$X^2–Y^2$							1.0000	0.1254	0.1353
Z^3								1.0000	0.0693
Z^2									1.0000

*The cross correlation coefficients of the shims from the acquired field reference matrix. Ideally, orthogonal shims should give approximately zero cross correlation since the ROI was taken to be a centered spherical region. The individual shim fields were normalized so that diagonal elements of $\mathbf{M^TM}$ were unity. Note the high degree of correlation between Z and Z^3.

tion. Spherical harmonics can also be used as basis functions, and in this case, for an off-center ROI, one can re-orthogonalize the shims by translating the frame of reference (13), thus eliminating the increased interaction of the shims in the basis functions. However, due to measurement noise from the subject and limited maximum currents from the shim amplifiers, the need for a regularization method may still arise whether one chooses spherical harmonics or, as we have done, basis functions based on measured fields.

The field map of the subject being shimmed is more vulnerable to errors than the field reference matrix since no averaging is performed. It is also subject to motion artifacts for in vivo studies. Equations [4]–[6] quantify the effect that field map errors have on the computed shim currents. Thus, the inability of the shimming procedure to reach its predicted RMS value after a single iteration is more likely to come from errors in the field map of the subject rather than the field reference matrix. In such cases, iteration of the shimming procedure can be performed to minimize errors and converge to a minimum residual norm. Typically, one or two iterations are sufficient for in vivo shimming (Fig. 5).

The predicted residual field after shimming represents field variations that are orthogonal to the basis functions; i.e., the field variations that cannot be removed by shimming for the given ROI. These residual field components will not necessarily be orthogonal to ideal spherical harmonics since the acquired field reference matrix is used instead as basis functions. Thus, it represents components that are orthogonal to the SVD. A closer examination of any unique characteristics of these residual field components can lead to the design of specialized shim coils (21).

Phase wraps in the acquired field map will result in a failure of the proposed shimming technique. This is dealt with in two ways. First, the TE difference in the field mapping acquisition is chosen to cover a bandwidth that is sufficiently wide for the vast majority of in vivo imaging ($\pm$ 250 Hz). Based on our extensive experience in in vivo shimming over the human head, this bandwidth is more than sufficient for robust shimming. In addition to the inherent bandwidth determined by the choice of ΔTE of 2 ms, the spiral pulse sequence also contains a spectral-spatial excitation pulse. The primary purpose of this feature is the suppression of all signals from spins with resonance frequencies shifted by more than 200 Hz from the nominal center frequency. This includes lipids as well as any water signals from very inhomogeneous regions. Since the shimming algorithm includes computing a mask based on the magnitude of the water image, signal from all spins with resonant frequencies greater than 200 Hz are eliminated and hence generate no undesirable phase wraps in the computed field maps.

CONCLUSIONS

We have presented a method of higher-order shimming using a regularized algorithm that provides increased numerical stability for in vivo shimming of arbitrary ROIs. The entire shimming procedure is implemented with a graphically-driven software package designed for use in a clinical environment.

ACKNOWLEDGMENTS

We thank David Clayton for proofreading the manuscript.

REFERENCES

1. Schneider E, Glover G. Rapid in vivo shimming. Magn Reson Med 1991;18:335–347.
2. Reese T, Davis T, Weisskoff R. Automated shimming at 1.5T using echo-planar image frequency maps. J Magn Reson Imaging 1995;5:739–745.
3. Irarrazabal P, Meyer CH, Nishimura DG, Macovski A. Inhomogeneity correction using an estimated linear field map. Magn Reson Med 1996; 35:278–282,
4. Spielman DM, Adalsteinsson E, Lim KO. Quantative assessment of improved homogeneity using high-order shims for spectroscopic imaging of the brain. Magn Reson Med 1998;40:376–382.
5. Jaffer FA, Wen H, Balaban RS, Wolff SD. A method to improve the B_0 homogeneity of the heart in vivo. Magn Reson Med 1996;36:375–383.
6. Gruetter R. Automatic, localized in-vivo adjustments of all first and second-order shim coils. Magn Reson Med 1993;29:804–811.
7. Shen J, Rycyna RE, Rothman DL. Improvements on an in-vivo automatic shimming method (fastermap). Magn Reson Med 1997;388:834–839.
8. Tropp J, Derby KA, Hawryszko C, Sugiura S, Yamagata H. Automated shimming of B_0 for spectroscopic imaging. J Magn Reson 1988;85:244–254.
9. Webb P, Macovski A. Rapid, fully automatic, arbitrary-volume in-vivo shimming. Magn Reson Med 1991;20:113–122.

10. Prammer MG, Haselgrove JC, Shinnar M, Leigh JS. A new approach to automatic shimming. J Magn Reson 1988;7:40–52.
11. Gruetter R, Tkac I. Improved sensitivity and speed for localized, subsecond shimming without a reference scan. In: Proceedings of the 7th Annual Meeting of ISMRM, Philadelphia, 1999. p 1768.
12. Kanayama S, Kuhara S, Satoh K. In-vivo rapid magnetic field measurement and shimming using single scan differential phase mapping. Magn Reson Med 1996;36:627–642.
13. Hoult DI. "Shimming" on spatially localized signals. J Magn Reson 1987;73:174–177.
14. Wedin PA. Perturbation theory for pseudo-inverses. BIT, 1973;13:217–232.
15. Tikhonov AN. Solution of incorrectly formulated problems and the regularization method. Soviet Math Dokl 1963;4:1035–1038.
16. Ekstrom MP, Rhodes RL. On the application of eigenvector expansions to numerical deconvolution. J Comput Phys 1974;14:319–340.
17. Hansen PC. The truncated SVD as a method for regularization. BIT 1987;27:534–553.
18. Hansen PC. Rank-deficient and discrete ill-posed problems. SIAM J Appl Math 1998;50.
19. Glover GH. Simple analytic spiral k-space algorithm. Magn Reson Med 1999;42:412–415.
20. Romeo F, Hoult DI. Magnet field plotting: analysis and correcting coil design. Magn Reson Med 1984;1:44–64.
21. Adalsteinsson E, Spielman DM. Dedicated shim coil design. In: Proceedings of the 6th Annual Meeting of ISMRM, Sydney, Australia, 1998. p 477.